Hybrid density functional theory band structure engineering in hematite

Zachary D. Pozun and Graeme Henkelman[a)]
Department of Chemistry and Biochemistry and the Institute for Computational Engineering and Sciences, University of Texas at Austin, 1 University Station A5300, Austin, Texas 78712-0165, USA

(Received 29 March 2011; accepted 18 May 2011; published online 14 June 2011)

We present a hybrid density functional theory (DFT) study of doping effects in α-Fe_2O_3, hematite. Standard DFT underestimates the band gap by roughly 75% and incorrectly identifies hematite as a Mott-Hubbard insulator. Hybrid DFT accurately predicts the proper structural, magnetic, and electronic properties of hematite and, unlike the DFT+U method, does not contain d-electron specific empirical parameters. We find that using a screened functional that smoothly transitions from 12% exact exchange at short ranges to standard DFT at long range accurately reproduces the experimental band gap and other material properties. We then show that the antiferromagnetic symmetry in the pure α-Fe_2O_3 crystal is broken by all dopants and that the ligand field theory correctly predicts local magnetic moments on the dopants. We characterize the resulting band gaps for hematite doped by transition metals and the p-block post-transition metals. The specific case of Pd doping is investigated in order to correlate calculated doping energies and optical properties with experimentally observed photocatalytic behavior. © *2011 American Institute of Physics*. [doi:10.1063/1.3598947]

I. INTRODUCTION

α-Fe_2O_3, commonly known as hematite, is a relatively inexpensive and easily synthesized[1] material that has a significant abundance in the earth's crust.[2] It has attracted significant research in lithium-ion batteries,[3–5] gas sensors,[6,7] catalysis,[8–11] environmental protection,[12,13] and Martian astrochemistry.[14–18]

In particular, hematite is a cost-effective material that has solar cell and photoelectrocatalytic applications.[19–21] In the design of highly efficient materials for these processes, a band gap that maximizes absorption of incident sunlight is highly desirable. A band gap on the order of 1.3-1.4 eV is ideal for maximum absorbance of sunlight. Hematite has an indirect band gap of ~2 eV (Ref. 22) and a direct optical gap of 2.7 eV,[23] and, consequently, presents an enticing opportunity for band gap tuning via doping.

Several experimental methods exist to rapidly scan potential doped structures for photocatalytic behavior. Lee *et al.*[24] have developed a scanning electrochemical microscopy method for rapidly identifying photocatalytic doped α-Fe_2O_3 bimetallics. They identify 30% Pd, 10% Eu, and 20% Rb as more photoactive than pure α-Fe_2O_3.[24] Other fast combinatorial methods include ink jet printing of metal nitrates onto conductive glass substrates,[25] spray pyrolysis onto glass electrodes,[26,27] and atmospheric pressure chemical vapor deposition.[28]

Although easy to synthesize and dope experimentally, hematite is difficult to model using the standard local density approximation (LDA) and related density functional theory (DFT) methods. X-ray absorption and emission spectra indicates that α-Fe_2O_3 is a charge transfer insulator.[29–32] The generalized-gradient approximation (GGA) in DFT underestimates the band gap by 75% as well as incorrectly positions the $3d$ orbitals such that it predicts a d-d Mott-Hubbard insulator.[33]

Standard GGA also underestimates the magnetic moments on the Fe centers. Hematite is an antiferromagnetic insulator below the Néel temperature of $T_N = 955$ K.[34] At the Morin temperature, $T_M = 260$ K, there is a magnetic phase transition in which the antiferromagnetic axis realigns.[35] The Fe centers are $3d^5$ with a distorted octahedral local environment that produces a high-spin crystal field splitting.[30] The experimentally measured magnetic moments are ~4.6-4.9 μ_B per atom.[36,37] GGA, however, predicts 3.4 μ_B per atom.[38]

The LDA/GGA band gap and magnetic moments can be corrected using both the LDA+U (Ref. 33) and GGA+U (Ref. 38) methods. These methods require an empirical parameter, the Hubbard U, that is adjusted in order to arrive at the proper gap. These methods provide reasonable agreement with experimental values when the U parameter is properly set; however, U is an atom- and d electron-specific parameter. In doped systems, the LDA+U method may provide reasonable results with respect to identifying localized states.[39] For band gap tuning, however, the atom- and d electron-specific nature of the method makes the resulting band gap unfavorably dependent upon a choice of a dopant U value that cannot be empirically chosen.

In contrast to the LDA/GGA methods, the Hartree-Fock (HF) method correctly produces a charge transfer semiconductor by correctly identifying the top of the valence band as O $2p$ states rather than Fe $3d$.[40] The HF method, however, significantly over-predicts the magnitude of the band gap. Hybrid functionals, which contain a fractional amount of exact HF exchange, are capable of arriving close to the experimental band gap for metal oxides such as ceria,[41] titania,[42] and a variety of others.[43] Hybrid functionals for band gap tuning have been applied by Yin *et al.* to titania.[44]

a)Electronic mail: henkelman@mail.utexas.edu.

In this work we present a band gap tuning via doping study and employ a hybrid functional to correctly model the localization of electrons without atom-specific empirical parameters that only directly act on d valence electrons. Our goal is to identify the dopants that lower the band gap of α-Fe_2O_3 by either raising the valence band edge or lowering the conduction band edge. We employ a hybrid functional that is able to correctly determine the band gap and other material properties for undoped hematite.

II. COMPUTATIONAL METHODS

A. Computational details

All calculations were performed using the Vienna *ab initio* simulation package (VASP),[45–48] a plane-wave implementation of DFT. The valence electrons were described in terms of Kohn-Sham (KS) (Refs. 49 and 50) single-electron orbitals and were expanded in a plane-wave basis with an energy cutoff of 300 eV. Core electrons were defined within the projector-augmented wave (PAW) methodology.[51,52]

Brillouin zone integration was expedited by using a finite-temperature Gaussian smearing function with $\sigma = 0.05$ eV. All atoms were allowed to relax until the net force per atom was less than 0.01 eV/Å or until the total electronic extrapolated free energy had converged to less than 0.5 meV change between ionic steps. The local densities of states (DOS) were calculated by projecting the KS wave functions onto atom-centered spherical harmonic functions within each atom's Wigner-Seitz radius.

Optical properties were calculated in the PAW framework by using the method of Gajdoš *et al.*[53] The 3×3 imaginary dielectric tensor is calculated in the random phase approximation using a summation over conduction bands. Each matrix element for a given angular frequency ω is given by[53]

$$\varepsilon^{(2)}_{\alpha\beta}(\omega) = \frac{4\pi^2 e^2}{\Omega} \lim_{\mathbf{q}\to 0} \frac{1}{\mathbf{q}^2} \sum_{c,v,\mathbf{k}} 2w_{\mathbf{k}} \delta(\epsilon_{c\mathbf{k}} - \epsilon_{v\mathbf{k}} - \omega) \times \langle u_{c\mathbf{k}+\mathbf{e}_\alpha q} \mid u_{v\mathbf{k}} \rangle \langle u_{c\mathbf{k}+\mathbf{e}_\beta q} \mid u_{v\mathbf{k}} \rangle^*, \quad (1)$$

where the vector $\mathbf{q}$ is a Brillouin zone wave vector and $\mathbf{e}_\alpha$ is a Cartesian unit vector. The indices c and v refer to conduction and valence band states. The real part, $\varepsilon^{(1)}_{\alpha\beta}$ is generated via a Kramers-Kronig transformation. Each ω-dependent tensor is generated in Cartesian space and the resulting matrix is diagonalized to yield the dielectric constants in the planes parallel and perpendicular to [0001].

The exchange-correlation (XC) contribution to the DFT energy was calculated using several distinct functionals. At the GGA level, the Perdew-Burke-Ernzerhof (PBE) functional was employed.[54,55] In contrast to the local GGA functional, the non-local exact exchange HF functional was applied using the PAW formalism of Paier *et al.*[56] The PBE0 (Ref. 57) hybrid functional, where the full XC energy is determined by

$$E_{\mathrm{XC}}^{\mathrm{PBE0}} = \tfrac{1}{4} E_{\mathrm{X}}^{\mathrm{HF}} + \tfrac{3}{4} E_{\mathrm{X}}^{\mathrm{PBE}} + E_{\mathrm{C}}^{\mathrm{PBE}}, \quad (2)$$

was also tested. The screened Heyd-Scuseria-Ernzerhof (HSE) hybrid functional was also applied.[58,59] In this functional, the Coulomb kernel is decomposed into short- and long-range components such that the total XC energy contribution smoothly transitions from PBE0 at short range to PBE at long range. For this work, $\mu = 0.2$ Å is set in order to conform with the HSE06 (Ref. 60) version of the functional.

B. Hematite structure

The lattice constants calculated within the GGA+U framework by Rohrbach *et al.*[38] were employed for all calculations. Due to the computational cost of hybrid functionals, full lattice relaxations were computationally intractable with the hybrid functionals. The lattice constants from GGA+U were selected due to their closeness to the experimental lattice constant and due to the similarities in the computational methodolgy.

α-Fe_2O_3 is a hexagonal corundum structure in space group $R\bar{3}c$.[61] The primitive cell is a rhombohedral cell with the lattice constant $a_{\mathrm{rhom}} = 5.474$ Å and an angle between vectors of $\alpha = 55.195^\circ$ when converted from the GGA+U structure. All of the Fe centers are crystallographically equivalent and occupy the (4c) Wyckoff position with the O centers occupying the (6e) position.[62] The primitive cell is shown in Fig. 1.

For DOS and optical property calculations, the 10-atom primitive cell was sampled with a 5×5×5 Monkhorst-Pack k-point mesh.[63] Due to the high accuracy required of DOS and optical calculations, the semicore $3p$ electrons were considered as valence for these calculations.

The 30-atom hexagonal representation of the unit cell has calculated lattice constants of $a = 5.067$ Å and $c = 13.882$ Å.[38] The hexagonal unit cell contains six Fe_2O_3 formula units arranged along [0001] in the order of O_3–Fe–Fe–O_3. The Fe–Fe distance within layers is shorter than the Fe–Fe distance between layers. The hexagonal unit cell is shown in Fig. 2.

For band gap tuning calculations, the unit cell was expanded along the $[10\bar{1}0]$ and $[01\bar{1}0]$ directions to form a 120-atom supercell whose Brillouin zone was sampled at the Γ point. The semicore p states for the d^6 and greater metals were all considered to be non-interacting core electrons and were treated in the PAW pseudopotentials.

The semicore p states were considered as valence for the d^5 and less transition metals. In order to determine the relative positions of the conduction band and valence band edges in relaxed structures, the semicore Fe p states were included as

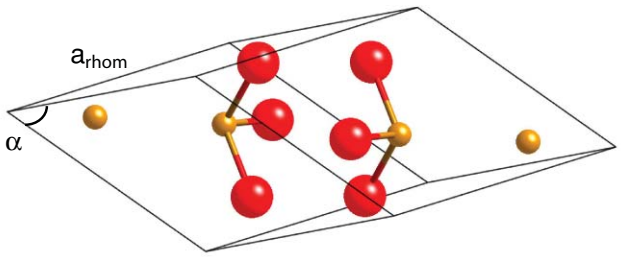

FIG. 1. The primitive cell of α-Fe_2O_3 with the only lattice constant labeled. The Fe atoms sit on the (4c) Wyckoff position and the O atoms sit at the (6e) position.

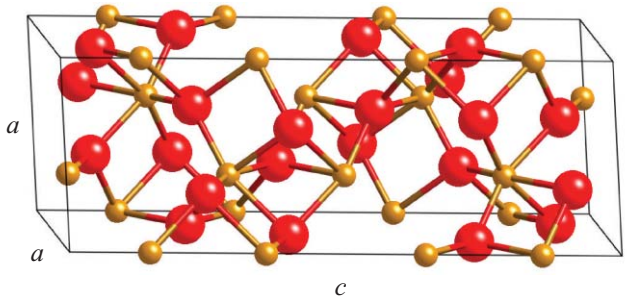

FIG. 2. The unit cell of α-Fe_2O_3 with the two principle axes labeled. The full unit cell contains six Fe_2O_3 formula units with the Fe centers ordered along [0001].

valence such that the lowest eigenvalue could be referenced between calculations.

The antiferromagnetic ordering along [0001] in the hexagonal representation and along [111] in the rhombohedral primitive cell is $+--+$ with opposing magnetic moments placed on the Fe–Fe centers separated by the short length. The proper antiferromagnetic ground state was verified by integrating the magnetic charge density within each atom's Wigner-Seitz radius.

III. RESULTS AND DISCUSSION

A. Comparison of standard functionals

The predictions of GGA (Ref. 38) and HF (Ref. 40) have each been demonstrated to accurately predict some electronic and physical properties of α-Fe_2O_3 and insufficiently predict others. We performed a comparison of the standard DFT functionals PBE, HSE06, and HF in order to compare the calculated properties with experiment and with a screened functional that contains 12% exact exchange, designated as HSE (12%). In order to rationally design doped semiconductors for photocatalytic purposes, a functional without atom-specific parameters, capable of modeling valence p states, and able to accurately predict magnetic, electronic, and optical properties is required.

The primitive cell of α-Fe_2O_3 contains four Fe atoms ordered along [111] with a short axis between pairs of Fe centers and a longer axis separating the pairs. Each Fe atom has six O centers surrounding it with a distorted octahedral geometry, whereby three of the Fe–O bonds have a shortened bond length.

The calculated bond lengths are shown in Table I. There is a strong trend that standard GGA-DFT tends to shorten the long axes and lengthen the short axes as the electronic states are delocalized across more atoms. With increasing exact exchange, the shorter bond lengths constrict and the longer bond lengths expand; these changes in the bond length allow the minimized structure to approach the experimental values.

TABLE I. Structural properties from standard functionals.

	PBE	HSE06	HF	HSE(12%)	Expt. (see Ref. 61)
Fe–Fe (A) [Å]	2.95	2.91	2.88	2.94	2.88
Fe–Fe (B) [Å]	3.99	4.03	4.06	4.00	3.98
Fe–O (A) [Å]	1.94	1.96	1.97	1.95	1.99
Fe–O (B) [Å]	2.15	2.13	2.11	2.14	2.06

TABLE II. Electronic, optical, and magnetic properties from standard functionals.

	PBE	HSE06	HF	HSE(12%)	Expt.
μ [μ_B/Fe atom]	3.60	4.16	4.60	4.16	4.64 (Ref. 37)
$E_{\text{band gap}}^{indirect}$ [eV]	0.67	3.41	15.58	1.95	2.0 (Ref. 22)
$E_{\text{band gap}}^{direct,\Gamma}$ [eV]	1.17	4.02	15.70	2.56	2.7 (Ref. 23)
$\epsilon^o(0)$	23.6	5.2	2.0	8.2	~6 (Ref. 64)
$\epsilon^e(0)$	19.1	4.7	2.0	6.8	~5 (Ref. 64)
Fe 3d center [eV]	−3.31	−5.36	−11.31	−4.31	~5 (Ref. 65)
O 2p center [eV]	−3.94	−3.29	−3.07	−3.41	~4 (Ref. 29)

The electronic, optical, and magnetic properties are significantly more sensitive to the choice of functional and the amount of exact exchange included. The Fe centers are formally Fe^{3+} with a high-spin d^5 valence with a $+--+$ ordering along [111] in the primitive cell. The total spin per atom, then, is $S = 5/2 = 5\ \mu_B$. Experimentally, however, the magnetic moment per atom is ~4.6 μ_B,[37] because not all spin-up charge or spin-down charge is located on a single Fe center. From Table II, it is apparent that GGA-DFT underestimates the localization of spin-up or spin-down charge on each Fe center, and that increasing the amount of exact exchange approaches the correct magnetic moment.

In terms of the electronic properties of the $+--+$ antiferromagnetic, high-spin ground state, DFT significantly underestimates the direct and indirect band gap. The HSE06 functional, which contains 25% exact exchange at short range and is pure GGA over long range, overestimates the band gap by approximately the same amount that pure GGA underestimates the gap. GGA incorrectly identifies hematite as a Mott-Hubbard insulator by placing the O 2p states lower in energy than the Fe 3d states. This error is corrected in all exact exchange functionals.

Hematite is an anisotropic optical medium with different dielectric responses along the a and c axes in the hexagonal unit cell. The response along both equivalent a axes is referred to as the ordinary wave and along c as the extraordinary wave. The static dielectric constants $\epsilon^o(0)$ and $\epsilon^e(0)$ are overestimated by standard DFT. The HS06 functional predicts the two constants better and increased amounts of exact exchange underestimate the static dielectric constants.

From the results presented in Tables I and II, the problem with the hybrid functionals becomes apparent. In contrast to the small-gap predictions of DFT, even the functionals with a small amount of exact exchange predict insulating behavior too strongly. We find that a functional with 12% exact exchange at short range that smoothly transitions, similar to HSE06, to pure PBE at long ranges accurately predicts nearly all experimental properties. Tables I and II show that this functional most reliably produces values near to the experimental values.

HSE (12%) predicts an indirect band gap of 1.95 eV, a direct gap at the Γ point of 2.56 eV, and the charge-transfer insulating behavior in accordance with spectroscopic evidence.

This functional does predict a greater degree of *p*-*d* hybridization than the DFT+U method; however, this behavior has been observed experimentally.[29,65] The method of adjusting the amount of exact exchange is similar to Janotti *et al.*[42] who applied 20% exact exchange to pure titania and to Yin *et al.*[44] who applied 22% exact exchange to doped titania.

In the HSE06 functional, the screening parameter μ is related to the distance $2/\mu$ at which the short-range exact exchange term becomes negligible. In the HSE06 functional, this distance is set to $\mu = 0.2$ Å^{-1}, which is the shortest screening distance recommended by Krukau *et al.*[66] Shortening this screening distance beyond the minimum would suggest a stronger decay in the short-range exchange that would reduce the exact exchange interaction between nearest- and second-nearest neighboring Fe centers. The screening distance set in HSE06—similarly applied in HSE(12%)—has been demonstrated to accurately model the material properties of a wide range of semiconductors.[58,60,66]

B. Doping hematite with transition metals

As predicted by ligand field theory (LFT), d^5 Fe centers coordinated to six ligands in an octahedral geometry will adopt a high-spin state such that each orbital contains a single, unpaired electron. As shown in Sec. III A, the local $S = 5/2$ spin environment on each Fe center is ordered $+ - -+$ along [0001] in the hexagonal unit cell. As noted by Velev *et al.*[67] in a DFT+U study of first-row dopants, any single substitution will break the antiferromagnetic symmetry.

Both the addition and removal of valence *d* electrons will lower the local magnetic moment. Second and third row transition metals, as predicted by LFT, have a significantly higher splitting between valence *d* states such that the low-spin configuration is adopted. In the low-spin octahedral environment, three t_{2g} orbitals are filled according to the Aufbau principle before the two e_g orbitals become occupied. This effect is shown in Fig. 3.

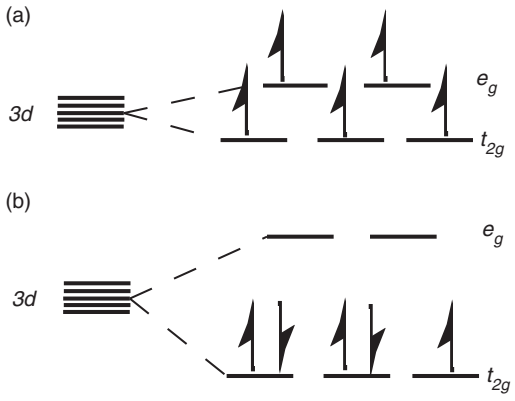

FIG. 3. The ligand field splitting diagram for a d^5 valence is shown for high and low spin environments. (a) Fe, in the first row, experiences low energy splitting between t_{2g} and e_g states such that the states are filled according to Hund's rule. (b) Ru and Os have a higher splitting between states such that the t_{2g} orbitals fill first according to the Aufbau principle.

1. High-spin 3d metal dopants

The results using the HSE (12%) functional are in qualitative agreement with the first-row transition metal study of Velev *et al.*[67] using DFT+U. Co, Ni, Cu, and Zn are all high-spin dopants such that electrons are incrementally added to half-filled 3*d* dopant-centered orbitals. These low-lying *d* states lie below the O 2*p* states near the Fermi level, so, as shown in Fig. 4, the HOMO is relatively unaffected. All of the band gap reduction occurs due to the lowering of the LUMO such that the resulting material behaves like a p-type semiconductor.

Beginning from Fe and moving toward Zn in Fig. 4, there is a monotonic decrease in the HOMO-LUMO gap with the exception of Ni. As previously noted, in LFT the octahedral coordination environment splits the five 3*d* orbitals into three degenerate t_{2g} orbitals and two higher energy e_g. In the case of Ni, the t_{2g} are 5/6 filled, which is a relatively high energy configuration. As such, there is a low-lying unoccupied LUMO state in the band gap that lowers the HOMO-LUMO gap. The addition of an additional electron in Cu fills this subshell and results in two degenerate, unoccupied e_g band gap states.

Unique among this trend, Zn adopts a Zn^{2+} formal oxidation state with all of its *d* orbitals filled and only two electrons donated to the O 2*p* band complex. Given that it is replacing a Fe^{3+} ion that has formally donated three electrons, a hole is introduced in the gap that is primarily centered in the O ligands around a neighboring Fe center. Zn is thus distinct from the trend in Co, Ni, and Cu where the band gap is primarily altered by incrementally pairing the *d* electrons and breaking the spin symmetry of the full supercell.

In the reverse trend in the first row moving from Fe toward Sc, it is the LUMO that is relatively unaffected and the HOMO that is thrust upward in energy. The band gap for Cr is relatively unshifted due to the stability of half-filling of each of the three t_{2g} orbitals and completely depopulating the two e_g orbitals. The same case is noted in Sc, which contains no 3*d* electrons; consequently, the band gap is essentially unaffected as compared to Fe.

In similar qualitative agreement with Velev *et al.*[67] and Bandyopadhyay *et al.*,[39] when used as a dopant, Ti takes a formal Ti^{4+} oxidation state. The excess donated electron primarily localizes on two nearby Fe centers with an energy lying

Fe Band Gap ΔHOMO ΔLUMO									
Sc 2.04 + 0.04 - 0.01	Ti 0.43 + 1.64 - 0.01	V 0.85 + 1.22 - 0.01	Cr 1.70 + 0.36 - 0.03	Mn 1.04 + 0.78 - 0.27	Fe 2.08 0.00 0.00	Co 1.41 + 0.11 - 0.56	Ni 0.53 + 0.11 - 1.44	Cu 1.16 + 0.05 - 0.88	Zn 0.86 - 0.20 - 1.03
Y 1.96 + 0.21 + 0.01	Zr 0.32 + 1.73 - 0.03	Nb 0.41 + 1.66 - 0.01	Mo 0.68 + 1.44 + 0.04	Tc	Ru 0.91 + 1.10 - 0.07	Rh 1.56 + 0.46 - 0.07	Pd 0.89 + 0.76 - 0.43	Ag 1.17 - 0.09 - 0.82	Cd 0.84 + 0.24 - 1.01
La	Hf 0.28 + 1.78 - 0.03	Ta 0.45 + 1.68 + 0.02	W 0.30 + 1.76 - 0.01	Re 0.44 + 1.62 - 0.02	Os 0.71 + 1.33 + 0.03	Ir 1.18 + 0.86 - 0.05	Pt 0.35 + 1.64 - 0.10	Au 1.50 + 0.39 - 0.19	Hg

FIG. 4. The band gaps and HOMO-LUMO shifts for transition metal dopants are shown. All shifts are calculated with respect to the undoped supercell. Energies are found by referencing the lowest eigenvalue of the non-interacting Fe *p* core state. All units are in eV.

in the band gap. This system behaves similar to an n-doped semiconductor with a small HOMO-LUMO gap where conduction may be possible by exciting the excess electron into hopping between Fe centers. Experimental evidence indicates that 4% Ti-doped hematite shows increased photocatalytic activity.[68]

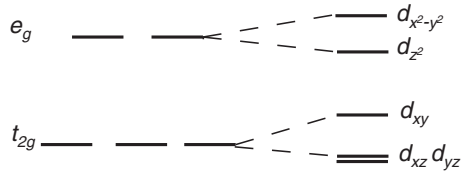

FIG. 5. The orbital splitting for Jahn-Teller distorted octahedral complexes is shown. Typical Jahn-Teller distortion arises in low-spin complexes where there is an unpaired electron in the e_g doubly degenerate orbitals.

2. Low-spin 4d and 5d metal dopants

In contrast to the dopants presented in Sec. III B 1, the splitting of the 4*d* and 5*d* orbitals in an octahedral environment, as predicted by LFT, is large enough to ensure that all spin complexes will be low-spin. This result indicates that the three degenerate t_{2g} orbitals will fill before the two degenerate e_g orbitals become populated. As shown in Fig. 4, although Ru and Os are isoelectronic in the valence with Fe, the antiferromagnetic symmetry of the supercell is broken. The local moments on Ru and Os correspond to 5/6 filling of the t_{2g} states and a relatively unshifted LUMO. The LUMO in both cases is a t_{2g} state lying at the bottom of the valence band complex.

In contrast, Mo and W each are d^3 in the valence, and Rh and Ir are d^6. These compounds benefit from the stability of half-filled and fully filled subshells, respectively. The t_{2g} HOMO states on the dopants lie in the band gaps. The HOMO-LUMO gap in Mo and W is relatively small and due to the higher energy, has half-filled states. Rh and Ir, which both have a full t_{2g} subshell, have no local magnetic moment on the dopant. Rh and Ir have larger HOMO-LUMO gaps due to the stability of the filled subshell. In these cases, the LUMO is still comprised of the Fe 3*d* states, so it is essentially unshifted.

Partial filling of the t_{2g} subshell is particularly unstable for the low-spin 4*d* and 5*d* metals. Similar to Ti, Hf adopts a Hf^{4+} oxidation state and donates an extra electron onto neighboring Fe centers. Unlike V, however, Nb and Ta take a Nb^{5+} and Ta^{5+} oxidation state and create two band gap states localized on nearby Fe centers. In the case of high-spin V, the oxidation state is V^{3+} with the two t_{2g} electrons localized on the V center.

Similar to the cases of Mo and W, Ag and Au both prefer to have a half-filled e_g subshell with two unfilled states lying in the band gap and centered on the dopant. Cd, however, adopts a Cd^{2+} oxidation state rather than having a 3/4-filling in the degenerate e_g levels. By taking the Cd^{2+} rather than Cd^{3+} oxidation state common to the other dopants, a LUMO hole is introduced in the band gap but is centered on adjacent Fe centers. Although Fig. 4 shows similar shifts in the LUMO for Ag and Cd, these dopants differ in where the hole is localized.

As shown in Fig. 5, unpaired electrons in degenerate orbitals are unstable and the local ligand field typically distorts as predicted by the Jahn-Teller effect.[69] Degeneracy in the e_g is significantly more likely to lead to Jahn-Teller distortions due to the fact that these orbitals point directly at the ligand field. In the low spin *d* metals, only Pd, Pt, Ag, Au, and Cd are potentially affected by this distortion. As previously noted, Cd overcomes this problem by taking a Cd^{2+} oxidation state, and Au and Ag both benefit by half-filling their e_g subshell.

The most interesting case, then, is Pd and Pt. Pd retains the Pd^{3+} oxidation state and places a single electron into a *d* state localized on the Pd center and with an energy lying in the band gap. The ligand field around the Pd dopant is Jahn-Teller distorted such that the orbital takes d_{z^2} symmetry. The overall HOMO-LUMO gap is entirely localized onto the Pd dopant. Pt, however, takes a Pt^{4+} oxidation state due to the Jahn-Teller instability of 1/4 filling of the two degenerate e_g states. In this case, the extra electron is localized on a nearby Fe center in a spin-down t_{2g} orbital. Figure 6 shows charge density isosurface for the band containing the localized electron as a result of the doping.

The local *d* DOS for the dopant atoms for the Ni, Pd, and Pt column is compared to a single Fe atom in an undoped crystal in Fig. 7. In the case of Ni, a high-spin d^7 center, the unoccupied spin down t_{2g} state, lies directly above the Fermi level and is very close to the valence band edge; this unoccupied orbital accounts for the significant lowering of the LUMO. In contrast, Pd has a localized state in the Jahn-Teller shifted d_{z^2} orbital lying directly below the Fermi level, so the HOMO is shifted up in energy compared to pure hematite.

As shown in Fig. 6, a Pt dopant localizes the electron in a t_{2g} orbital of a nearby Fe center rather than add to a Pt-localized e_g that would be Jahn-Teller susceptible. As shown in Fig. 7, the Fermi level for a Pt dopant shifts toward the conduction band edge. The Pt-projected DOS shows a small band gap state indicating that the electron localized on the nearby Fe^{2+} center is slightly hybridized with the Pt 5*d* orbitals.

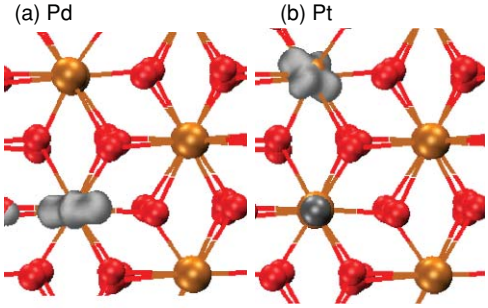

FIG. 6. The localized band gap electronic state is shown for Pd and Pt dopants, which are each circled in light blue. (a) The electron is entirely localized on the Pd center and clearly displays the Jahn-Teller and LFT-predicted d_{z^2} symmetry. (b) The electron is localized on a nearby Fe center instead of the Pt dopant. The extra electronic state has the LFT-predicted t_{2g} symmetry.

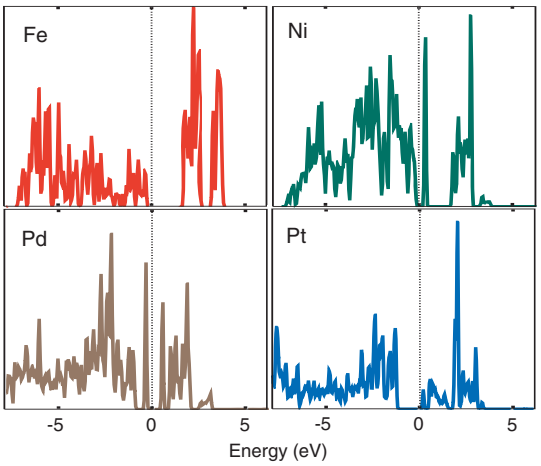

FIG. 7. The local d-DOS for Ni, Pd, and Pt are plotted and compared to an undoped Fe atom. In all cases, the zero of energy is the Fermi level for that particular crystal. All units are in eV.

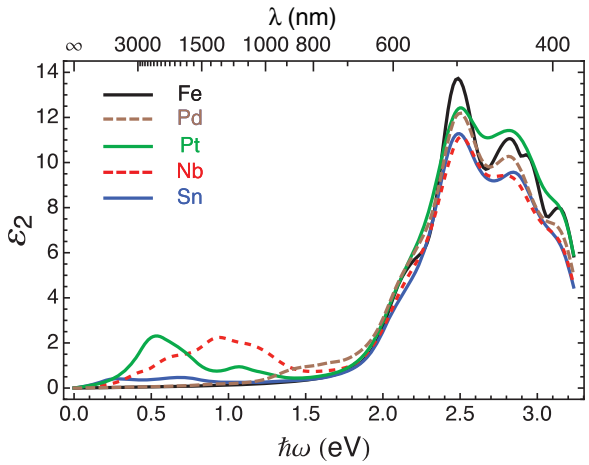

FIG. 9. The optical response for a singly doped 120-atom hematite supercell is shown for various dopants. The plotted optical responses are along the axis with the largest dielectric response.

C. Doping hematite with the *p*-block metals

Dopants that are p-block in valence are a unique opportunity for hybrid functionals. In the DFT+U method, on-site correlations are specific to d electrons, whereas hybrid functionals are capable of treating on-site correlations in the same manner for p electrons as d. Dopants of the p-block post-transition metals and metalloids are summarized in Fig. 8.

The column of Al, Ga, In, and Tl behaves nearly identically to the Sc column in the transition metal dopants. Each, upon adopting a D^{3+} oxidation state, has only a small effect on the overall HOMO-LUMO gap.

The cases of Ge, Sn, and Pb are more interesting from a materials design perspective. Each of the chosen metals adopts a D^{4+} oxidation state and creates a carrier localized very close to the valence band minimum. Both Ge^{4+} and Sn^{4+} show little on-site hybridization with the extra electron, which is instead localized on nearby Fe centers. The small resulting HOMO-LUMO gaps are such that these systems would behave akin to an n-type semiconductor with a relatively small amount of energy required to excite the carrier into the valence band complex. Pb^{4+} shows greater hybridization with the adjacent Fe and O atoms such that the gap state has a greater degree of delocalization. Consequently, the gap state sits farther below the Fermi level.

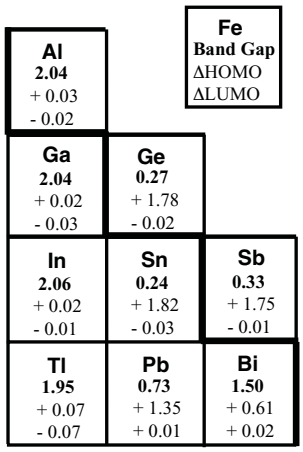

FIG. 8. The band gaps and HOMO-LUMO shifts are shown for p-block metal dopants. Only the p-block metals and metalloids are considered. All units are in eV.

The column of Sb and Bi behaves similar to the column of Pd and Pt in terms of differing in oxidation states and the degree of electron localization at the dopant. Sb adopts a Sb^{5+} oxidation state, which means that it donates two electrons to nearby iron centers. These extra two electrons that are transferred to adjacent iron centers are relatively high in energy, which accounts for the narrow HOMO-LUMO gap. In contrast, Bi has a Bi^{3+} oxidation state, such that the two HOMO electrons are localized on the Bi dopant with a significant charge delocalization onto the nearby O centers.

D. Optical properties of doped structures

Although the HOMO-LUMO gap and related material properties provide a prediction for photocatalytic performance, the full dielectric response is a more complete predictor of optical behavior. From Eq. (1), the frequency-dependent complex dielectric function can be calculated by a summation over conduction bands. Each term in the 3×3 matrix contains an overlap integral between valence band and conduction band states. Although the HOMO-LUMO gap may be on the same order as the incident photon, a poor overlap between states will result in a poor dielectric response.

The optical properties of selected dopants from Figs. 4 and 8 are tested for absorption in the range of photon energies from 0 to 3.26 eV (380 nm). The maximum imaginary frequency-dependent dielectric response, $\epsilon_2(\omega)$, is shown for several different dopants in Fig. 9.

From Figs. 4 and 8, Pd, Pt, Nb, and Sn have relatively narrow HOMO-LUMO gaps. These dopants may be separated into two groups based on the localization of the gap-state electrons. In Pd and Sn, the electrons are localized on the dopant; however, Pt and Nb both localized the electrons on a nearby Fe center and create a Fe^{2+} state.

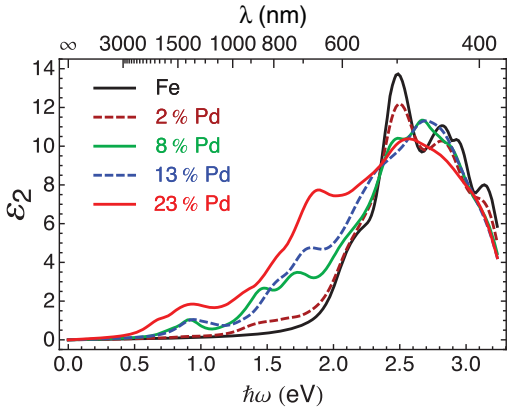

FIG. 10. The optical response for Pd-doped hematite is shown for increasing dopant concentration. The imaginary dielectric is plotted for various concentrations of Pd dopants from the infinite wavelength limit to the end of the visible range.

Figure 9 shows that the two dopants that create Fe^{2+} states show a significantly stronger dielectric response than the two dopants where the extra electrons are localized on the dopant. Both Nb and Pt have a large dielectric response in the very long wavelength limit; however, these two dopants have essentially the same response curve as pure hematite in the visible range of 750-390 nm. The Pd dopant shows an elevated response at essentially the onset of the visible regime.

E. The effect of increasing Pd dopant concentration

As noted by Lee *et al.*,[24] the peak photocurrent for Pd doping occurs experimentally in a material made of ∼70/30 Fe/Pd. In Sec. III B 2, we note that both the HOMO and LUMO are located on the Pd dopant with a gap that falls in the infrared. The dielectric response of a single Pd dopant in a 120 atom supercell, a 98/2 Fe/Pd material, shows an increased dielectric response in the visible range as compared to pure hematite. Here, we investigate the optical properties and energetics of higher doping concentrations.

As a relatively noble metal, Pd does not typically oxidize and its single stable oxide form is PdO.[70] In practical terms for hematite doping, the instability of Pd_2O_3 indicates that as the dopant concentration increases, the overall stability of the doped hematite structure is destabilized. High concentrations of Pd_2O_3 are energetically unfavorable. As noted by Lee *et al.*,[24] large doping concentrations of Pd likely contain regions of PdO or pure Pd, rather than a doped hematite structure.

In the limit of low Pd doping, where the $Pd_{2x}Fe_{2-x}O_3$ structure may be produced experimentally, the optical response to the concentration is significantly altered as a function of doping concentration. The frequency-dependent imaginary dielectric response, $\epsilon_2(\omega)$, is shown in Fig. 10.

From Fig. 10, a clear trend emerges where absorption significantly increases in the 1.25-2.0 eV range that has effectively no optical response in pure hematite. This region comprises a significant portion of the visible regime that is significant for solar cell applications. A doping concentration of 23% Pd shows a heightened optical response across the entire visible spectrum and into the infrared. Materials with doping concentrations on this approximate concentration have been shown experimentally[24] to have peak photocatalytic activity. From Fig. 10, it is clear that a material on this doping concentration absorbs strongly across the entire visible range and is also not too energetically unstable to be produced experimentally.

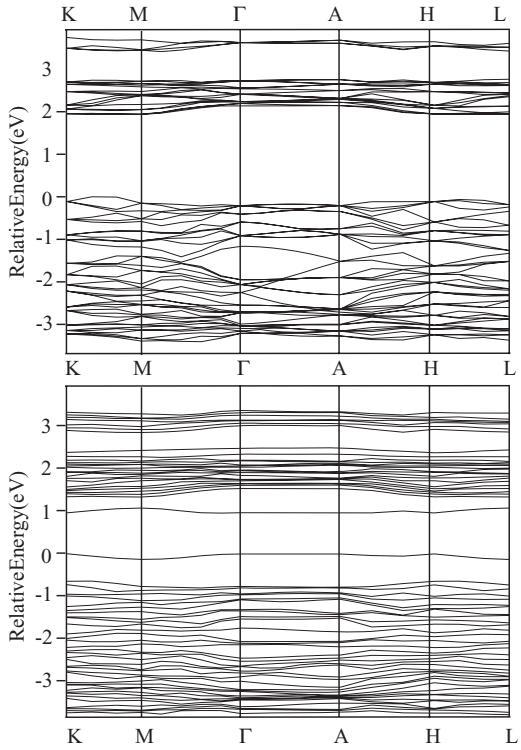

FIG. 11. The band structures for pure hematite (upper) and 8% Pd-doped (lower) are plotted across high-symmetry directions in the Brillouin zone. Here, we use the conventions K = (1/3, 1/3, 0), M = (1/2, 0, 0), Γ = (0, 0, 0), A = (0, 0, 1/2), H = (1/3, 1/3, 1/2), and L = (1/2, 0, 1/2). The zero of energy in each case is the energy of the highest occupied band.

The optical absorption spectra in Fig. 10 are calculated using the method of summation over bands detailed by Gajdoš *et al.*[53] The band structures for undoped hematite and 8% Pd-doped hematite are shown in Fig. 11. In the lower band structure plot, the Pd dopant states are clearly visible with transitions localized on the Pd center with a gap of ∼0.89 eV as well as transitions in the 1.5-2.5 eV range from the Pd dopant HOMO onto the Fe 3*d* LUMO bands.

IV. CONCLUSIONS

Due to its relatively low cost, ease of synthesis, and band gap on the approximate order of the maximum in the solar radiation spectrum, hematite is a highly attractive material for solar cell applications. Due to the strong correlation effects from the Fe 3*d* electrons, however, it is a challenging material for computational study. We demonstrate that hybrid functionals are capable of accurately predicting the material, electronic, and optical properties of pure hematite, α-Fe_2O_3.

A screened hybrid functional with 12% exact exchange predicts a band gap that is in accordance with experimental observations. This functional also correctly identifies

hematite as a charge-transfer, rather than the Mott-Hubbard insulator with the proper static dielectric constant and correct uniaxial optical behavior.

Hematite is a material that is highly symmetric locally on the Fe centers and on the whole crystal. Each Fe^{3+} ion is a high-spin d^5 center, so all d orbitals are half-filled. In the crystal the spins are aligned $+ - -+$ along the [0001] direction. These levels of symmetry are broken by doping with all potential dopants; therefore, the resulting HOMO-LUMO gap is due to the addition of states into the band gap. We characterize the nature of these states using hybrid-DFT and traditional ligand field theory.

We show that the optical response of the system to solar spectrum radiation must shift due to the shrinking HOMO-LUMO gap. We calculate the optical response of hematite due to several different dopants and show that the response is larger, but occurs outside of the visible range, for dopants which localize excess electrons onto Fe^{2+} centers.

Finally, we explore the case of increased doping of Pd into Fe_2O_3 and find correlation with previous experimental results. Increased doping of Pd results in an increasing energy cost to replace a Fe center with Pd such that high doping levels in an experimental system will likely result in localized concentrations of PdO and pure Pd. At concentrations on the order of 77/23 Fe/Pd, the system exhibits a strong optical response across the entire solar spectrum.

ACKNOWLEDGMENTS

Computational resources were provided from the Texas Advanced Computing Center (TACC) and the National Energy Research Scientific Computing Center (NERSC). The authors wish to thank Ting Yan for her help with interpreting experimental data.

[1] N. T. Hahn, H. Ye, D. W. Flaherty, A. J. Bard, and C. B. Mullins, ACS Nano **4**, 1977 (2010).
[2] A. Miyashiro, Geochim. Cosmochim. Acta **28**, 717 (1964).
[3] C. Wu, P. Yin, X. Zhu, C. OuYang, and Y. Xie, J. Phys. Chem. B **110**, 17806 (2006).
[4] S. Zeng, K. Tang, T. Li, Z. Liang, D. Wang, Y. Wang, and W. Zhou, J. Phys. Chem. C **111**, 10217 (2007).
[5] Z. Wu, K. Yu, S. Zhang, and Y. Xie, J. Phys. Chem. C **112**, 11307 (2008).
[6] W. S. Choi, H. Y. Koo, Z. Zhongbin, Y. Li, and D.-Y. Kim, Adv. Funct. Mater. **17**, 1743 (2007).
[7] X. Gou, G. Wang, J. Park, H. Liu, and J. Yang, Nanotechnology **19**, 125606 (2008).
[8] E. Liger, L. Charlet, and P. van Cappellen, Geochim. Cosmochim. Acta **63**, 2939 (1999).
[9] F. Herrera, A. Lopez, G. Mascolo, P. Albers, and J. Kiwi, Applied Catalysis B: Environmental **29**, 147 (2001).
[10] H.-H. Huang, M.-C. Lu, and J.-N. Chen, Water Res. **35**, 2291 (2001).
[11] O. Shekhah, W. Ranke, A. Schüle, G. Kolios, and R. Schlögl, Angew. Chem., Int. Ed. **42**, 5760 (2003).
[12] P. Li, D. E. Miser, S. Rabiei, R. T. Yadav, and M. R. Hajaligol, Appl. Catal., B **43**, 151 (2003).
[13] R. Mecozzi, L. di Palma, D. Pilone, and L. Cerboni, J. Hazard. Mater. **B137**, 886 (2006).
[14] P. R. Christensen, R. V. Morris, M. D. Lane, J. L. Bandfield, and M. C. Malin, J. Geophys. Res. **106**, 23873 (2001).
[15] D. C. Catling and J. M. Moore, Icarus **165**, 277 (2003).
[16] I. Fleischer, D. G. Agresti, G. Klingelhöfer, and R. V. Morris, J. Geophys. Res. **115**, E00F06 (2010).
[17] A. S. Madden, V. E. Hamilton, M. E. E. Madden, P. R. Larson, and M. A. Miller, Earth Planet. Sci. Lett. **298**, 377 (2010).
[18] A. Johnson, L. Pratt, T. Vishnivetskaya, S. Pfiffner, R. Bryan, E. Dadachova, L. Whyte, K. Radtke, E. Chan, S. Tronick, G. Borgonie, R. Mancinelli, L. Rothschild, D. Rogoff, D. Horikawa, and T. Onstott, Icarus **211**, 1162 (2011).
[19] N. Beermann, L. Vayssieres, S.-E. Lindquist, and A. Hagfeldt, J. Electrochem. Soc. **147**, 2456 (2000).
[20] G. K. Mor, H. E. Prakasam, O. K. Varghese, K. Shankar, and C. A. Grimes, Nano. Lett. **7**, 2356 (2007).
[21] T. Lopes, L. Andrade, H. A. Ribeiro, and A. Mendes, Int. J. Hydrogen Energy **35**, 11601 (2010).
[22] S. Mochizuki, Phys. Status Solidi A **41**, 591 (1977).
[23] J. A. Glasscock, P. R. F. Barnes, I. C. Plumb, A. Bendavid, and P. J. Martin, Thin Solid Films **516**, 1716 (2008).
[24] J. Lee, H. Ye, S. Pan, and A. J. Bard, Anal. Chem. **80**, 7445 (2008).
[25] M. Woodhouse, G. S. Herman, and B. A. Parkinson, Chem. Mater. **17**, 4318 (2005).
[26] C. J. Sartoretti, B. D. Alexander, R. Solarska, I. A. Rutkowska, J. Augustynski, and R. Cerny, J. Phys. Chem. B **109**, 13685 (2005).
[27] W. B. Ingler, Jr., and S. U.M. Khan, Int. J. Hydrogen Energy **30**, 821 (2005).
[28] A. Kay, I. Cesar, and M. Grätzel, J. Am. Chem. Soc. **128**, 15714 (2006).
[29] A. Fujimori, M. Saeki, N. Kimizuka, M. Taniguchi, and S. Suga, Phys. Rev. B **34**, 7318 (1986).
[30] R. J. Lad and V. E. Henrich, Phys. Rev. B **39**, 13478 (1989).
[31] F. Ciccacci, L. Braicovich, E. Puppin, and E. Vescovo, Phys. Rev. B **44**, 10444 (1991).
[32] G. Dräger, W. Czolbe, and J. A. Leiro, Phys. Rev. B **45**, 8283 (1992).
[33] G. Rollmann, A. Rohrbach, P. Entel, and J. Hafner, Phys. Rev. B **69**, 165107 (2004).
[34] C. W. Searle and G. W. Dean, Phys. Rev. B **1**, 4337 (1970).
[35] F. J. Morin, Phys. Rev. **78**, 819 (1950).
[36] E. Krén, P. Szabó, and G. Konczos, Phys. Lett. **19**, 103 (1965).
[37] J. M. D. Coey and G. A. Sawatzky, J. Phys. C **4**, 2386 (1971).
[38] A. Rohrbach, J. Hafner, and G. Kresse, Phys. Rev. B **70**, 125426 (2004).
[39] A. Bandyopadhyay, J. Velev, W. H. Butler, S. K. Sarker, and O. Bengone, Phys. Rev. B **69**, 174429 (2004).
[40] M. Catti, G. Valerio, and R. Dovesi, Phys. Rev. B **51**, 7441 (1995).
[41] J. L. F. Da Silva, M. V. Ganduglia-Pirovano, J. Sauer, V. Bayer, and G. Kresse, Phys. Rev. B **75**, 045121 (2007).
[42] A. Janotti, J. B. Varley, P. Rinke, N. Umezawa, G. Kresse, and C. G. Van de Walle, Phys. Rev. B **81**, 085212 (2010).
[43] J. Muscat, A. Wander, and N. M. Harrison, Chem. Phys. Lett. **342**, 397 (2001).
[44] W.-J. Yin, H. Tang, S.-H. Wei, M. M. Al-Jassim, J. Turner, and Y. Yan, Phys. Rev. B **82**, 045106 (2010).
[45] G. Kresse and J. Hafner, Phys. Rev. B **47**, 558 (1993).
[46] G. Kresse and J. Hafner, Phys. Rev. B **49**, 14251 (1994).
[47] G. Kresse and J. Furthmuller, Comput. Mater. Sci. **6**, 15 (1996).
[48] G. Kresse and J. Furthmüller, Phys. Rev. B **54**, 11169 (1996).
[49] P. Hohenberg and W. Kohn, Phys. Rev. **136**, 864 (1964).
[50] W. Kohn and L. J. Sham, Phys. Rev. **140**, 1133 (1965).
[51] P. E. Blöchl, Phys. Rev. B **50**, 17953 (1994).
[52] G. Kresse and D. Joubert, Phys. Rev. B **59**, 1758 (1999).
[53] M. Gajdoš, K. Hummer, G. Kresse, J. Furthmuller, and F. Bechstedt, Phys. Rev. B **73**, 045112 (2006).
[54] J. P. Perdew, K. Burke, and M. Ernzerhof, Phys. Rev. Lett. **77**, 3865 (1996).
[55] J. P. Perdew, K. Burke, and M. Ernzerhof, Phys. Rev. Lett. **78**, 1396 (1997).
[56] J. Paier, R. Hirschl, M. Marsman, and G. Kresse, J. Chem. Phys. **122**, 234102 (2005).
[57] C. Adamo and V. Barone, J. Chem. Phys. **110**, 6158 (1999).
[58] J. Heyd, G. E. Scuseria, and M. Ernzerhof, J. Chem. Phys. **118**, 8207 (2003).
[59] J. Heyd and G. E. Scuseria, J. Chem. Phys. **121**, 1187 (2004).
[60] J. Heyd, G. E. Scuseria, and M. Ernzerhof, J. Chem. Phys. **124**, 219906 (2006).
[61] L. Pauling and S. Hendricks, J. Am. Chem. Soc. **47**, 781 (1925).
[62] M. Blanchard, M. Lazzeri, F. Mauri, and E. Balan, Am. Mineral. **93**, 1019 (2008).

[63]H. J. Monkhorst and J. D. Pack, Phys. Rev. B **13**, 5188 (1976).
[64]C. T. Chen and B. D. Cahan, J. Opt. Soc. Am. **71**, 932 (1981).
[65]N. S. McIntyre and D. G. Zetaruk, Anal. Chem. **49**, 1521 (1977).
[66]A. V. Krukau, O. A. Vydrov, A. F. Izmaylov, and G. E. Scuseria, J. Chem. Phys. **125**, 224106 (2006).
[67]J. Velev, A. Bandyopadhyay, W. H. Butler, and S. Sarker, Phys. Rev. B **71**, 205208 (2005).
[68]N. T. Hahn and C. B. Mullins, Chem. Mater. **22**, 6474 (2010).
[69]H. A. Jahn and E. Teller, Proc. R. Soc. London, Ser. A **161**, 220 (1937).
[70]M. Peuckert, J. Phys. Chem. **89**, 2481 (1985).